The axisymmetric collapse of a mixed patch and internal wave generation in uniformly stratified rotating fluid

Amber M. Holdsworth[1] and Bruce R. Sutherland[2,1,a]
[1]*Department of Earth and Atmospheric Sciences, University of Alberta, Edmonton, Alberta T6G 2E3, Canada*
[2]*Department of Physics, University of Alberta, Edmonton, Alberta T6G 2E1, Canada*

We present an experimental and numerical investigation of the effect of Coriolis forces on the axisymmetric collapse of a uniform mixed region in uniformly stratified fluid. Laboratory experiments were performed on a rotating table in which a mixed patch contained initially in a hollow cylinder was released and so excited internal waves whose properties were analyzed using synthetic schlieren. Numerical simulations restricted to an axisymmetric geometry were run with the experimental parameters to confirm the accuracy of the code and the validity of the axisymmetric approximation. The simulations were then run in larger domains and with wide-ranging parameters exploring the dependence of wave generation upon rotation and the aspect ratio of the mixed patch. Internal waves are found to be generated from the circumference of a shallow aspect-ratio mixed patch, with the radial and vertical wavelengths scaling as the mixed-layer depth. In rotating fluid, the energy spectrum revealed that pairs of wavepackets were generated, one with near-inertial frequencies and one with frequencies near the buoyancy frequency. Energy transport due to the waves was most significant during the first 6 wave periods. However, for very low Rossby number Ro ~ 0.1, internal wave generation continued over relatively longer times as a consequence of undulations of the geostrophically adjusting mixed patch. © 2015 AIP Publishing LLC. [http://dx.doi.org/10.1063/1.4919850]

I. INTRODUCTION

Because of its size and large heat capacity, the oceans comprise an important part of the Earth's climate system. But it is not well understood how heat from the surface is transported via diapycnal mixing across the thermocline into the oceanic abyss. Assuming a uniform global upwelling throughout the ocean abyss, an average vertical eddy diffusivity of 10^{-4} m^2/s (a quantity sometimes referred to as 1 Munk) is required to maintain the observed thermal structure.[1–4] However, observations indicate that the background diffusivity in the abyss is an order of magnitude smaller. The additional mixing is attributed largely to locally enhanced transient mixing resulting from interactions of the barotropic tide with coastal regions and submarine topography. Dye release experiments,[5] microstructure measurements,[6,7] and satellite altimeter data[8] have confirmed that the action of the barotropic tide near suitably large topography can excite internal waves that provide a pathway for the cascade of energy from large to small scale. As well as the tide, another important external energy source results from surface wind stress due to passing storms. This also constitutes a potentially significant source of internal waves and mixing.[3] The waves may be generated due to induced near-inertial interfacial waves and geostrophic currents,[9,10] stationary or sheared turbulence,[11–13] or intrusions resulting from the collapse of mixed regions.[14,15] The purpose of this study is to examine the last of these circumstances, extending previous work[15] by considering the influence of Coriolis forces and the effect of shallow aspect ratios of the mixed region. The work

---

a)Email: bruce.sutherland@ualberta.ca. URL: http://www.ualberta.ca/~bsuther.

    27, 056602-1

thus provides better insight into internal wave generation by horizontally wide but vertically thin mixed regions below storms and, in particular, below tropical cyclones (hurricanes and typhoons).

Although tropical cyclones are transient events, recent studies have shown there may be an important source of energy for ocean mixing.[16–18] They typically lower the sea surface temperature[19] by 1−3 °C, but have also been observed to lower it by up to 9 °C if slow-moving. Emanuel[18] demonstrated that a substantial amount of the ocean heating required to drive the poleward heat flux may be accounted for by localized mixing due to tropical cyclones. These storms are responsible for as much as 15% of peak ocean heat transport[17] and are one plausible mechanism for generating some of the diapycnal mixing necessary to drive the meridional overturning circulation.[16] Liu, Wang, and Huang[20] estimated that tropical cyclones on average increase the potential energy of the ocean at a rate of 0.05 TW.

These studies focused on the dynamics of the upper-ocean response to tropical cyclones. The ocean beneath them has been observed to mix to several hundred metres depth[21] leaving cold water wakes[22] that return to near pre-storm conditions over a period of lasting weeks to months through the process of re-stratification.[18] The near-surface may restratify in part due to the differential absorption of sunlight with depth. But in the darkness below 100 m, the dynamics of buoyantly driven horizontal flows, known as intrusive gravity currents or intrusions, must also play a role.

Lock-release laboratory experiments with non-rotating, uniformly stratified ambient fluid have examined the evolution of two-dimensional intrusions in long rectangular tanks[23–26] and of intrusions that spread radially after release from a cylindrical lock.[15,27] Of these, the experiments designed to examine wave generation found that internal waves were excited during the initial collapse of the lock-fluid.[15,24] The wave frequencies were found to be moderately below the buoyancy frequency, whereas the wavelength and amplitude were set by the depth of the mixed region. Because the waves transported only about 2% of the initial available potential energy (APE) of the mixed patch, their generation did not significantly affect the evolution of the intrusion. When applied to oceanographic circumstances, 2% of the substantial energy associated with a mixing region beneath storms is a significant source of the energy for the internal waves generated by the collapsing mixed region that could be associated with mixing at depth. However, being limited to the study of mixed patches with near unity width-to-depth aspect ratio and without considering Coriolis effects, the extension of the experiment results to the ocean was suggestive at best.

Although the process of geostrophic adjustment of a collapsing mixed patch in the low Rossby number regime has been well studied,[28] there are relatively few experimental and numerical studies examining the influence of moderate rotation upon radially spreading gravity currents and intrusions.[29–32] In laboratory experiments for which the Rossby deformation radius was significantly larger than the radius of the initial mixed patch, the collapsing fluid was found to propagate radially while increasing its azimuthal speed in the anticyclonic direction until reaching its maximum radial extent set by the deformation radius.[30,32] The fluid then reversed its direction, flowing radially inward and accumulated near the tank centre. This mass of fluid then exhibited a second outward pulse which propagated radially outward to a maximum radius before flowing inward once more. The process continued each time losing energy until the flow reached a geostrophically balanced state. Altogether, studies of intrusions in rotating stratified fluid have focused upon the evolution of the intrusion and not the generated internal waves.

In one of the first studies that indirectly examined internal waves generated by a collapsing mixed patch in rotating stratified fluid, Lelong and Sundermeyer[33] performed simulations designed to gain insight into the observed anomalously large lateral dispersion of tracers in the Coastal Mixing and Optics experiment. The patch itself was assumed to result from an internal wave breaking event, though modelling such breaking was not a part of their study. During the adjustment of the slumping patch to a geostrophically balanced lens, their simulations showed that high frequency waves were excited during the initial slumping of the patch and low frequency waves were excited as the lens became balanced. They found that the greatest fraction of initial available potential energy was transferred to kinetic energy associated with the balanced lens if the Rossby number was unity, meaning that the lateral extent of the mixed patch was comparable to the Rossby deformation radius.

The work presented here focuses specifically upon the energetics of internal waves excited by a collapsing mixed patch. The setup of laboratory experiments, the description of analysis techniques,

and the results are described in Sec. II. The setup and analysis of numerical simulations restricted to an axisymmetric geometry are described in Sec. III. Therein, we show that the structure of the waves observed in experiments is well reproduced by the numerical model. With this check performed on the validity of the model, we then present simulations of the collapse of a mixed patch in situations more relevant to the ocean. From this, we develop empirical predictions for the structure and amplitude of the waves, and so relate the energy of the wave field relative to the initial available potential energy of the system. Finally, in Sec. IV, we extend our results to the consideration of oceanic internal waves generated by tropical cyclones.

II. LABORATORY EXPERIMENTS

A. Setup

The experimental setup is shown in Figure 1. Experiments were performed in a square tank measuring 50 cm on each side which itself was situated on a 1 m diameter rotating table (Australian Scientific Instruments).

While stationary (not rotating), the "double-bucket" technique[34] was used to fill the tank with salt-stratified fluid such that the density increased linearly from top to bottom over a total depth of $H \simeq 40$ cm. Samples of the fluid in the tank were extracted by syringe at a sequence of depths and measured using a densitometer (Anton Paar DMA4500). From this, we confirmed that the density profile, $\bar{\rho}(z)$, was linear. The tank was then gradually put into solid body rotation. Spin-up in a stratified fluid is significantly more complicated than that in uniform density fluid because stratification impedes Ekman pumping. An impulsive spin-up leads to recirculation zones in the bottom edge of the tank[35] and significant vertical vorticity would develop along the four corners of our square tank. To inhibit such mixing, we gradually increased the rotation rate, first rotating at approximately 0.05 s^{-1} for half an hour, then incrementally increasing the rotation by steps of $\simeq 0.05$ s^{-1}, and waiting half an hour between steps until the desired rotation rate was reached. The typical time for this process was 12 h in total. In comparison, the time scale for viscous diffusion from the tank side walls to the interior is of the order 11 h.

Once in solid body rotation at the desired rotation rate, density samples were taken once more. Despite the obvious development of columnar vortices in corners of the tank during each spin-up phase, we found that the density profile remained linear except in the bottom few centimeters of the tank. Because our interest lay in the dynamics near the surface and mid-depth in the tank, the partially mixed fluid near the tank bottom did not affect our measurements of mixed region collapse and internal wave generation.
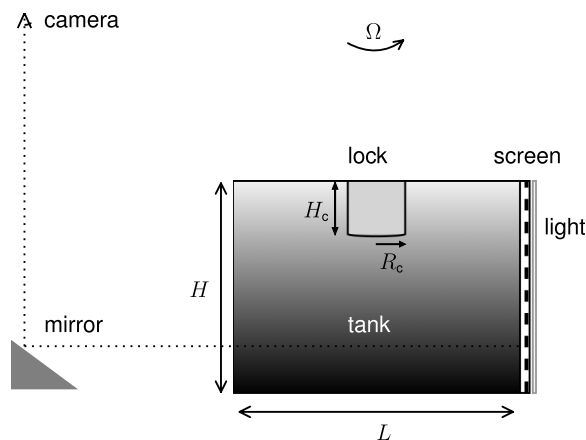

FIG. 1. Schematic of the experiment showing a cubical tank filled with uniformly stratified fluid situated on a rotating table. Internal waves were visualized using synthetic schlieren, whereby a camera looks downward to an angled mirror that permits a side view through the tank to an image printed on an illuminated screen on the opposite side of the tank. Fluid is mixed within a cylinder of radius R_c and depth H_c below the surface at the center of the tank.

From the final measurements of density at different depths, we found the best-fit line and so computed the corresponding squared buoyancy frequency, $N^2 = -(g/\rho_0)\, d\bar{\rho}/dz$, in which g is gravity and ρ_0 is a characteristic density taken to be that of fresh water. In the experiments reported upon here, N ranged from $1.57\,\text{s}^{-1}$ to $1.77\,\text{s}^{-1}$. The rotation rate ranged from $\Omega = 0.03\,\text{s}^{-1}$ to $0.45\,\text{s}^{-1}$, corresponding to inertial frequencies ranging from $f = 0.06\,\text{s}^{-1}$ to $0.90\,\text{s}^{-1}$.

A hollow acrylic cylinder of radius $R_c = 5.3$ cm was suspended above the centre of the tank and, in the frame of the rotating apparatus, it was lowered until its bottom extended below the surface of the ambient fluid to a depth of H_c, which ranged between 5.2 cm and 15 cm. The fluid within the cylindrical lock was then mixed with an oscillating mechanical stirrer until the density was uniform to a depth H_m, moderately smaller than H_c. In most experiments, we added a small amount of dye to the mixed fluid in the cylindrical lock to visualize the intrusion that resulted when the cylinder was extracted vertically. The concentration of dye was so small that it did not significantly affect the density of the lock-fluid. Density measurements of the lock-fluid, ρ_L, were used to estimate the value of H_m by relating ρ_L to the depth where the ambient fluid had the same density. H_m was taken to be twice this neutral-buoyancy depth. The extent of the dyed fluid in the lock provided a visual measurement of the mixed-layer depth. Depending upon the mixing process, this differed from H_m by up to 2 cm. Typical mixed layer depths ranged from $H_m = 5$ to 15 cm.

As established in previous experiments of intrusions in uniformly stratified non-rotating fluid, the intrusion speed is set by N and H_m. In particular, for sufficiently high (width-to-depth) aspect-ratio locks, the measured speed of intrusions from partial-depth cylindrical lock-release experiments[27,32] is moderately below the predicted rectilinear speed[36] of $U = NH_m/8$. Also based upon experiments examining internal wave generation by axisymmetric intrusions in non-rotating fluid, the wave frequency and wavelength are set by N and H_m, respectively. On this basis, we expect the Reynolds number for wave propagation is appropriately defined by $\text{Re} = NH_m^2/\nu$, in which ν is the kinematic viscosity. The Reynolds number for the intrusion is about an order of magnitude smaller. In our experiments, because Re ranged from 3.3×10^3 to 4.4×10^4, we do not expect that viscosity played an important role influencing the formation and evolution of the intrusion and internal waves over the first few buoyancy periods in which our analyses took place.

Estimating the initial intrusion speed to be $NH_m/8$, the Rossby deformation radius is defined in terms of the ambient stratification and the depth of the mixed region to be $R_d = NH_m/8f$, which is the ratio of the characteristic intrusion speed to the inertial frequency. The Rossby number based upon the initial radius of the mixed patch (R_c) is thus written as

$$\text{Ro} = \frac{1}{8}\frac{N}{f}\frac{H_m}{R_c} = \frac{R_d}{R_c}. \tag{1}$$

This ranged between 0.3 and 2.3 in rotating experiments.

We used axisymmetric synthetic schlieren[37,38] to measure the structure and amplitude of internal waves generated by the collapsing mixed region. In general, internal waves stretch and compress isopycnal surfaces. Because the index of refraction of salt water varies with salinity, light rays bend differentially as they pass through the wave field. And so, looking through the side of tank, an image on the other side will appear to distort as a consequence of internal waves passing between the image and viewer.

In the setup of our experiments, the image screen was composed either of black and white horizontal lines having thickness 3 mm or of randomly positioned dots. In both cases, the image was illuminated with a fluorescent light sheet (Electric Vinyl, Inc.) secured directly behind it. To extend the distance between the observer and screen in the rotating system, a digital camera (SONY DCR-TRV6 CCD) was positioned well above the table surface oriented to look down upon an angled mirror situated at the opposite side of the tank from the image screen. The total distance from the camera to the tank wall was 165 cm. During an experiment, the camera recorded the apparent displacement of lines or dots from the image. In the former case, sub-pixel deflections of lines could be detected by a digital camera, providing sensitive measurements of small displacements. In the latter case, the displacements of dots were determined using the open-source software called UVMAT (developed by Sommeria, Gostiaux, and Moreau at LEGI, University of Grenoble). This implemented a method called Correlation Image Velocimetry (CIV) that relied on direct cross correlations between image

pairs of pattern boxes to track the dots in the image. Like synthetic schlieren with lines, CIV involved tracking apparent displacements of the image screen. However, CIV measured horizontal as well as vertical displacements. Although providing more displacement information, in practice, we found the signals were noisier because the correlation algorithm required dots to displace significantly more than a fraction of a pixel to provide a coherent signal. With respect to analysis of internal waves, we were able to determine frequency and (radial) wavenumber spectra from CIV analyses. However, we relied on the results from images using horizontal lines to determine wave amplitudes.

Assuming the disturbance field within the tank was axisymmetric, we used a simple matrix inversion to compute the disturbance field from the measured image displacement fields.[15,39] Explicitly, we computed the gradient of the fluctuation density field, $\nabla\rho$. In particular, from its vertical component, we derived the change in the squared buoyancy frequency due to the waves, $\Delta N^2(r,z,t) = -(g/\rho_0)\partial\rho/\partial z$, and we computed its time derivative,

$$N_t^2 \equiv -\frac{g}{\rho_0}\frac{\partial^2\rho}{\partial t\,\partial z}, \tag{2}$$

from successive images taken 0.033–0.067 s apart. Examining this field had the advantage of filtering slowly evolving perturbations excited during the initial collapse while enhancing disturbances due to internal waves which evolved over relatively fast time scales. Conveniently for qualitative interpretation, the N_t^2 field for monochromatic internal waves is in phase with the vertical displacement field.

B. Qualitative results

After the cylinder containing the mixed fluid was extracted vertically, the mixed region was observed to collapse, propagating radially outward at its neutral buoyancy depth. This is shown in Figure 2. After two buoyancy periods (Fig. 2(a)), the mixed region propagated radially outward from the cylinder wall at $R_c = 5.3$ cm to radius 18 cm moving along its neutral buoyancy depth at $z = 34$ cm, a distance $H_m/2 \simeq 7$ below the surface. The half-depth of the intrusion was approximately 2 cm along its length, although it was somewhat deeper within the radius of the initial mixed region before collapse. This thinning and radial spreading of the intrusion was also observed in non-rotating experiments.[15] The effects of rotation were evident one buoyancy period later at $t = 3T_b$, corresponding approximately to one inertial period after the cylinder was extracted (Fig. 2(b)). As observed previously in gravity current and intrusion experiments with moderate Rossby number,[30,32] the intrusion halted its advance reversed direction and evolved into a lens shape. At later times, the lens expanded and then contracted again, repeating this process periodically until equilibrium was reached. From a top view (not shown, but see Fig. 12 of Holdsworth, Barrett, and Sutherland[32]), the mixed patch was observed to rotate anticyclonically as it spread outward in the rotating ambient. While contracting, its relative vorticity became smaller again. But throughout the expansion and contraction, the collapsed fluid never became cyclonic. Though not examined explicitly, the ambient above and below the collapsed fluid is expected through potential vorticity conservation to become more cyclonic as the mixed patch first collapses and less cyclonic as the mixed patch contracts. In experiments with greater rotation, the intrusion propagated radially over a smaller distance before contracting, consistent with the smaller deformation radius in those experiments.

Though not apparent by eye, a digital camera discerned sub-pixel distortions of the image of black and white lines in the top panels of Figure 2. From this, the N_t^2 field due to internal waves was computed, as shown in the bottom panels of Figure 2. In constructing the displayed N_t^2 fields, we inverted the image-displacement field to the left and right of $x = 0$ to get the radius-dependent wave field on either sides of the centreline. We then averaged the two results to get the assumed azimuthally symmetric internal wave field. For conceptual convenience, the images shown in Figures 2(c) and 2(d) have been reflected about the $r = 0$ axis. What is clear from both images is that lines of constant phase have a near fixed angle with the vertical, suggesting that the collapsing mixed patch generates waves in a narrow frequency range. Furthermore, the waves appear to be excited continually even after three buoyancy periods. The generation of waves with frequencies moderately below N has been observed before in non-rotating experiments.[15,24] However, the continuous excitation of internal
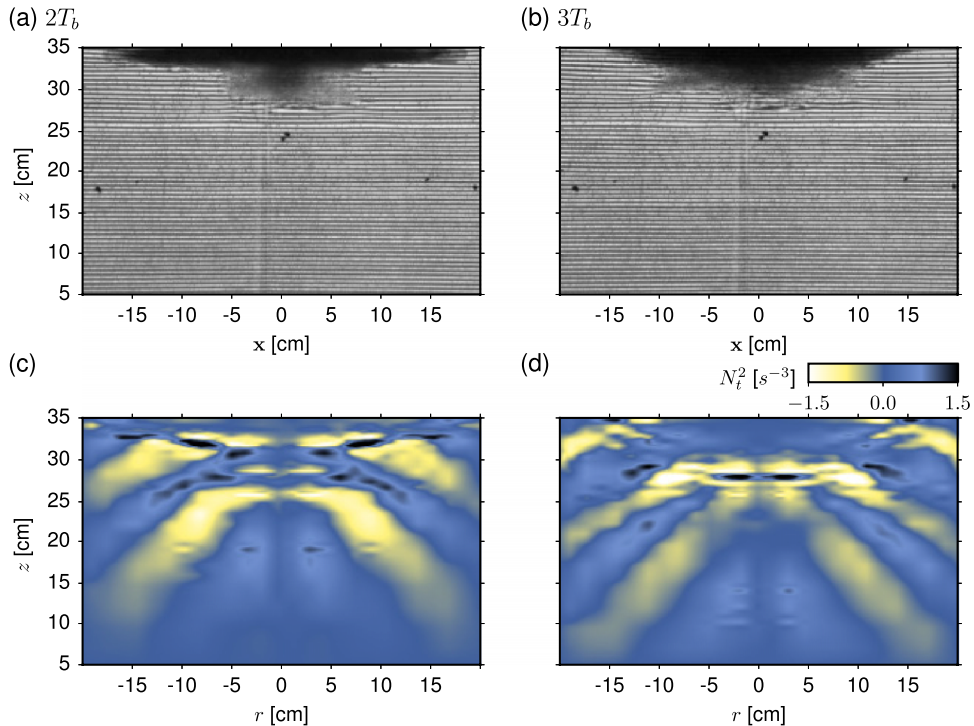
FIG. 2. Side view snapshots of an experiment taken at times (a) $2T_b$ and (b) $3T_b$ after the cylinder was extracted, and in (c) and (d), the corresponding internal wave field computed from the apparent displacements of horizontal lines at these two times. Here, $T_b = 2\pi/N$ is the buoyancy period. The internal wave field is represented by values of the N^2_t field with values indicated above (d). In this experiment, $N = 1.77$ s^{-1}, $H = 40.6$ cm, $H_m = 14$ cm, and $f = 0.502$ s^{-1}. The vertical axis is set with $z = 0$ at the bottom of the tank. Note that the top of each frame corresponds to the approximate neutral buoyancy depth; the actual surface is situated 5.6 cm above.

waves apparently is a consequence of the repeated expansion and contraction of the mixed patch, a process that takes place at the inertial frequency. In what follows, we will show that internal waves are in fact generated in two different frequency ranges, one set by N and the other set by f.

C. Internal wave structure: Analysis methods and results

In most of our analyses of the internal waves, we examined radial time series of the N^2_t field. From a sequence of images, such as those shown in Figures 2(c) and 2(d), we extracted the disturbance field at a fixed vertical level z just below the mixed region and recorded how the successive radial slices evolved in time. The result is shown in Figure 3 for two experiments with comparable values of N and H_m but with no rotation in Figure 3(a) and with $f = 0.502$ s^{-1} in Figure 3(b). Ignoring the discrepancies due to image resolution, the most significant difference between the time series is that the relative amplitude of the wave field is larger for the non-rotating case compared to the rotating case. In both the experiments, the wave periods and (radial) wavelengths are comparable, though in the non-rotating case, the phase-lines are somewhat curved, indicating slower radial advance of crests and troughs further from the source.

Following, Holdsworth, Decamp, and Sutherland,[15] each radial time series was decomposed as a Fourier-Bessel series according to

$$N^2_t(r,t) = \sum_{n=0}^{N} \sum_{m=0}^{M} A_{N^2_t}(k_n, \omega_m) J_0(k_n r) e^{-\iota \omega_m t}, \tag{3}$$

in which it is understood that the actual field is a real part of the right-hand side expression. Here, the radial wavenumber, $k_n = \alpha_n/R$, is given in terms of $R = L/2$, the tank half-width, and α_n, the successive zeroes the zeroth order Bessel function of the first kind, $J_0(r)$. The frequency is
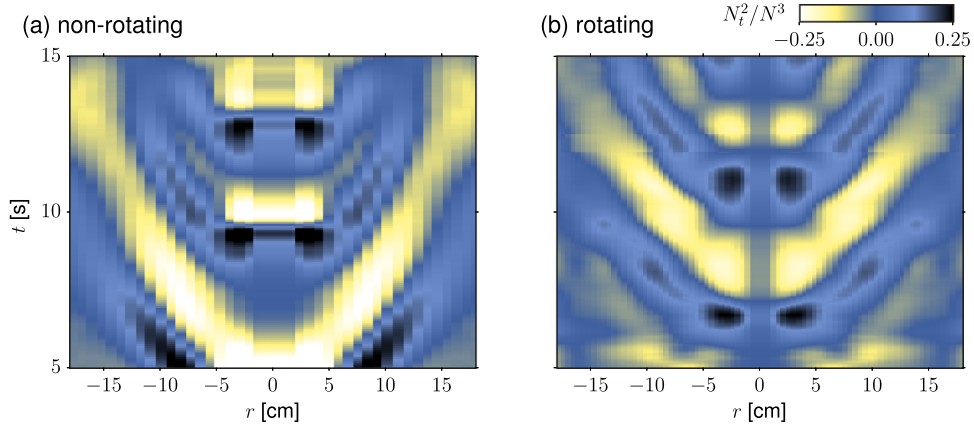
FIG. 3. Radial times series of the N_t^2 field normalized by N^3 determined from (a), a non-rotating experiment with $N = 1.53$ s^{-1}, $H = 45$ cm, $H_m = 14$ cm and from (b), the rotating experiment shown in Fig. 2. In both cases, the time series were constructed from a horizontal slice taken at $z = 15$ cm below the surface (1 cm below the base of the mixed region). Both time series begin 5 s after the start of the experiment in order to exclude image noise from the extraction of the cylinder.

$\omega_m = (2\pi/T)m$, in which T is the duration of the time series. For each $k = k_n$ and $\omega = \omega_m$, the vertical wavenumber, k_z, can be deduced from the dispersion relation,

$$\omega^2 = \frac{N^2 k^2 + f^2 k_z^2}{k^2 + k_z^2} = N^2 \cos^2\theta + f^2 \sin^2\theta, \tag{4}$$

in which θ is the angle formed between lines of constant-phase and the vertical

$$\theta = \cos^{-1}\sqrt{\frac{\omega^2 - f^2}{N^2 - f^2}}. \tag{5}$$

Explicitly, the vertical wavenumber as it depends upon radial wavenumber and frequency is

$$k_z = k\tan\theta = k\sqrt{\frac{N^2 - \omega^2}{\omega^2 - f^2}}, \tag{6}$$

with the sign taken to be positive corresponding to waves transporting energy downward.

To avoid transient start-up time and wave reflections from the side walls of the tank at late times, the analyses were performed between times $2T_b$ and $2T_b + 2T_w$, in which T_w is the characteristic wave period estimated by examination of the radial time series. Unlike analyses which use a double Fourier series in Cartesian space and time (appropriate for waves in a rectangular geometry), the decomposition of the radial disturbance field into Bessel functions in (3) means that the radial advance of phase lines in time can be captured only by an appropriate superposition of Bessel modes. Thus, although the waves in most experiments appeared to be quasi-monochromatic, their frequency and radial wavenumber spectra were found to be somewhat broader than their counterparts found in experiments of intrusion-generated waves in long rectangular tanks.[24] Nonetheless, we were able to determine the peak of the spectra through a series of parabolic fits. For the frequency peak, a frequency spectrum was constructed from a time series of N_t^2 at fixed radius r and a parabola was fit to the power of three frequencies about the largest power. The central frequency, $\omega_\star$, occurred where the parabola was largest. Averaging the central frequencies determined from all radial and vertical time series resulted in a single characteristic peak frequency, $\overline{\omega}_\star$. The standard deviation provided an estimate of the error. Likewise, the radial wavenumber peak was found by forming successive parabolic fits to power series constructed from Bessel transforms at fixed time. This gave the characteristic peak radial wavenumber, $\overline{k}_\star$, and its error.

Figure 4(a) plots the relative internal wave frequency $\overline{\omega}_\star/N$ against the relative radial wavenumber $\overline{k}_\star H_m$, in which H_m is the mixed layer depth. The values measured in laboratory
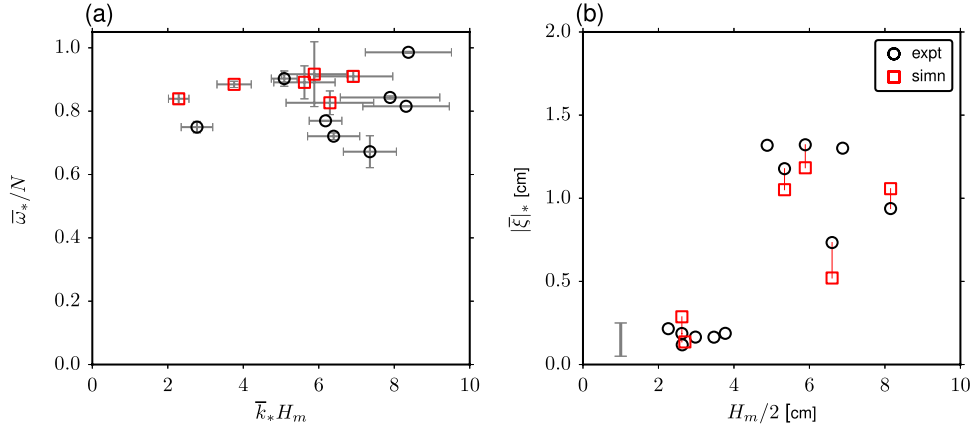
FIG. 4. (a) Peak spectral frequency normalized by the buoyancy frequency plotted against the peak spectral radial wavenumber multiplied by the mixed-layer depth and (b) the maximum vertical displacement amplitude plotted against the half-depth of the mixed region as determined for a range of laboratory experiments (circles) and corresponding numerical simulations (squares). Error bars in (a) indicate the width of the spectral peaks. The vertical lines in (b) connect laboratory experiment data with data from numerical simulations run with the same parameters as the experiments. A typical vertical error bar is shown in the lower-left corner of this plot.

experiments are indicted by open circles with error bars indicating the width of the spectral peak with respect to both frequency and wavenumber.

For wide-ranging experiments with different mixed layer depths and background rotation rates, the relative frequency of generated waves was found to lie within a range $0.67 \lesssim \overline{\omega}_\star/N \lesssim 0.99$. The range is moderately elevated from that found in the non-rotating rectilinear intrusion experiments of Sutherland, Chow, and Pittman,[24] who found $0.6 \lesssim \overline{\omega}_\star/N \lesssim 0.8$. The range is also somewhat broader than that found in the non-rotating axisymmetric intrusion experiments of Holdsworth, Decamp, and Sutherland,[15] who found that internal waves were generated with frequencies about $0.8\,N$. As we will show through the results of numerical simulations presented in Sec. III, inertial oscillations of the collapsing lock-fluid generate secondary waves with near inertial frequencies and these, superimposed with the high frequency waves detected more easily by synthetic schlieren, act to broaden the frequency spectrum.

In our experiments, after the cylinder was extracted, the predominant motion was a radial outward flow at depth $H_{\mathrm{m}}/2$ below the surface and radial inward flows of the ambient into the lock occurring near the surface and the base of the mixed region. In effect, this created a disturbance in the ambient stratified fluid with vertical wavelength set by H_{m}. Through (6) and the observation that ω lay in a relatively narrow frequency band, one might expect the radial flows to excite a downward propagating internal wave whose horizontal wavelength also depends upon H_{m}. Figure 4(a) shows that the relative horizontal wavenumber lies in the range $2.1 \lesssim \overline{k}_\star H_{\mathrm{m}} \lesssim 8.2$. Though wider, the range is comparable with that found in non-rotating rectilinear and axisymmetric intrusion experiments.[15,24] Alternately, if the mixed layer depth is large compared to its radius, one might expect that vertical rather than horizontal motion of the collapsing lock fluid would directly excite internal waves such that R_{c}, rather than H_{m}, should set the horizontal scale of the waves. Indeed, when scaled by R_{c}, we found the relative radial wavenumber to lie in the moderate range $2.7 \lesssim \overline{k}_\star R_{\mathrm{c}} \lesssim 5.2$. Of course the experiments were performed with a limited range of H_{m} between 5 and 15 cm and with R_{c} fixed at 5.3 cm. The numerical results in Sec. III make it clear that the horizontal scale of the waves is set by the larger of H_{m} and R_{c}.

From the Fourier-Bessel decomposition of the radial time series of N^2_t field (3) and the polarization relations appropriate for axisymmetric internal waves, listed in Table I, other fields of interest can be determined. In particular, using (6), the vertical displacement field is

$$\xi(r,t) = \sum_{n=0}^{N} \sum_{m=0}^{M} -\left(\frac{1}{k_n \omega_m N^2} \sqrt{\frac{\omega_m^2 - f^2}{N^2 - \omega_m^2}} \right) A_{N^2_{t},nm} \, J_0(k_n r) e^{-\imath \omega_m t}, \tag{7}$$

TABLE I. Polarization relations for the vertical displacement (ξ), (azimuthal) stream function (ψ), time change in the perturbed squared buoyancy (N_t^2), vertical velocity (w), radial velocity (u), azimuthal velocity (v), and pressure (p). The vertical wavenumber is given in terms of the radial wavenumber, k, and frequency, ω, by (6). It is understood that the actual fields are the real part of the right-hand side of the expressions.

Structure	Amplitude relation to A_ξ
$\xi = A_\xi J_0(kr)\, e^{\iota(k_z z - \omega t)}$	
$\psi = A_\psi J_1(kr)\, e^{\iota(k_z z - \omega t)}$	$A_\psi = -i\frac{\omega}{k} A_\xi$
$N_t^2 = A_{N_t^2} J_0(kr)\, e^{\iota(k_z z - \omega t)}$	$A_{N_t^2} = -k_z \omega N^2 A_\xi$
$w = A_w J_0(kr)\, e^{\iota(k_z z - \omega t)}$	$A_w = -\iota\omega A_\xi$
$u = A_u J_1(kr)\, e^{\iota(k_z z - \omega t)}$	$A_u = -\omega\frac{k_z}{k} A_\xi$
$v = A_v J_1(kr)\, e^{\iota(k_z z - \omega t)}$	$A_v = -f\frac{k_z}{k} A_\xi$
$p = A_p J_0(kr)\, e^{\iota(k_z z - \omega t)}$	$A_p = \iota\rho_0 \frac{\omega^2 k_z}{k^2} A_\xi$

in which $A_{N_{t,nm}^2} \equiv A_{N_t^2}(k_n, \omega_m)$ are the amplitudes of each radial wavenumber-frequency mode of the N_t^2 field, and it is understood that the actual vertical displacement is the real part of the right-hand side of (7).

Like the N_t^2 field, the vertical displacement field was the largest near $r = 0$ immediately below the mixed region where the waves could be distinguished from inertial oscillations of the mixed patch. Away from the base of the mixed patch, the maximum vertical displacement was found to decrease with increasing radius and vertical distance below the mixed region.

To find the maximum vertical displacement amplitude, $|\bar{\xi}|_\star$, successive radial profiles of the vertical displacement field, $\xi(r)$, were found at fixed z and t for $r \geq R_c$. We assumed the profile was modelled well by a radially shifted Bessel function, $J(r) \equiv AJ_0(k(r + r'))$, in which $k = \bar{k}_\star$ was the empirically measured radial wavenumber at the spectral peak. The radial shift was necessary because the generated waves were not standing modes but propagated outwards radially in time. Effectively, the phase shift kr' plays the role of the phase-shift in time, $-\omega t + \phi_0$, for waves propagating radially with phase speed ω/k. In terms of the asymptotic structure of zeroth order Bessel functions, the structure is approximately represented by $r^{-1/2} \cos(kr - \omega t + \phi_0)$.

By regression, we then found the best-fit values of the shift r' and amplitude A. This procedure was repeated for times between $2T_b$ and $2.5T_b$. In all cases, the analysis was performed on data taken at a vertical distance 5 cm below the mixed region. This was deemed to be sufficiently close to the source to be representative of the amplitude of the waves upon generation but not so close that the collapse and oscillations of the mixed patch obscured the signal due to waves alone. The average of the measured values of A was taken to be the maximum vertical displacement amplitude $|\bar{\xi}|_\star$.

Values of $|\bar{\xi}|_\star$ versus the half-depth of the mixed layer are plotted as open circles in Figure 4(b). Although there is some scatter in data, generally we find that the vertical displacement of the waves increases with increasing mixed-layer depth, as anticipated. However, given the variability in the data, it is unclear whether $|\bar{\xi}|_\star$ varies linearly with H_m.

D. Energy transport

The vertical transport of energy across a horizontal area of radius R is $\mathcal{F}_E(z) = \int_0^{2\pi} \int_0^R wp\, r\, dr\, d\theta$, in which w is the vertical velocity field and p is the pressure field. Because energy transmission is transient during the initial collapse and consequent inertial oscillations associated with the mixed region, we characterized the relative energetics of the waves through time-integrating the area-integrated flux to determine the energy. From the amplitudes $A_{N_{t,nm}^2}$ of the N_t^2 field and using the polarization relations, the energy transported between times T_1 and T_2 is

$$E = \int_{T_1}^{T_2} \mathcal{F}_E\, dt = \frac{\pi}{8} \frac{R^2}{N^4} (T_2 - T_1)\rho_0 \sum_{n=0}^{N} \sum_m \frac{\omega_m}{k_n^3} \sqrt{\frac{\omega_m^2 - f^2}{N^2 - \omega_m^2}} |A_{N_{t,nm}^2}|^2 J_1(\alpha_n)^2,$$
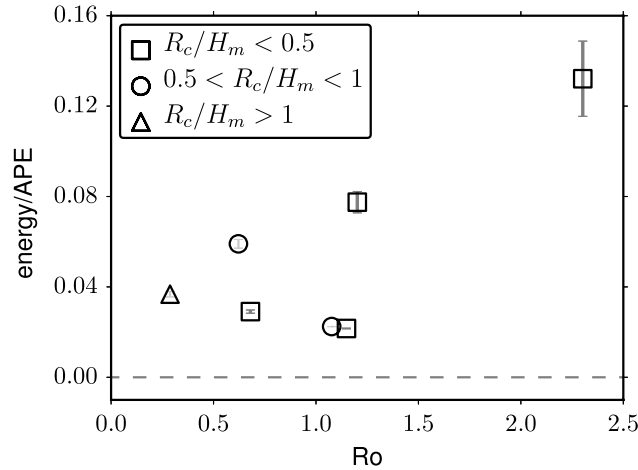
FIG. 5. Relative energy transported across the depth 5 cm below the bottom of the mixed region between times T_b and $T_b + 2T_w$ after the cylinder was extracted in laboratory experiments. Energy is given relative to the initial available potential energy and values are plotted against the Rossby number. Different symbols denote the aspect ratio of the lock-fluid as indicated in the legend. The indicated error bars are set primarily from errors in the measured wave amplitudes.

in which α_n are the zeroes of $J_0(r)$ and the sum over m is restricted to values for which $f < \omega_m < N$. Time integration was performed over two wave periods following one buoyancy period ($T_1 = T_b$, $T_2 = T_b + 2T_w$), a range during which the transport was substantial and wave reflections from the tank boundaries did not result in destructive interference of the signal. This energy-calculation procedure was applied to radial time series taken between 4 and 6 cm below the depth of the mixed-region and the result averaged to give the mean energy associated with waves passing 5 cm below the mixed region over two wave periods.

Figure 5 plots the measured energies normalized by the initial APE of the system associated with the mixed fluid in the lock. Explicitly, the initial available potential energy is given in terms of the initial total density and the ambient density, $\bar{\rho}(z)$,

$$\text{APE} = \iiint (\rho|_{t=0} - \bar{\rho}) \, gz \, dV \simeq \frac{\pi}{12} \rho_0 N^2 R_c^2 H_m^3, \qquad (8)$$

in which the last expression assumes the lock fluid has uniform density ρ_L over a depth H_m and radius R_c and ρ_L is the average of the ambient density over the depth of the lock fluid. The figure shows that 0.5%–13% of the initial APE was converted to energy associated with downward propagating internal waves. The largest percentage occurred for the large Rossby number experiment, with Ro $\simeq 2.3$, and the relative energy transport was consistent with the corresponding non-rotating experiments of Holdsworth, Decamp, and Sutherland.[15] In experiments with Rossby numbers less than unity, the energy associated with downward propagating internal waves was between 1% and 4% of the initial available potential energy. The results showed no obvious dependence upon lock aspect ratio, R_c/H_m, which varied between 0.39 and 1.2. However, it is well known that a mixed region collapsing in a rotating frame does not release all of its available potential energy to the ambient. The system evolves to geostrophic balance in which the mixed patch becomes an anticyclonic lens with associated available potential and kinetic energies. Just how much energy remains in the balanced lens and how much emanates as waves depend upon radius of the initial mixed patch compared with the Rossby deformation radius,[33] which in turn depends upon the Rossby number Ro given by (1). At fixed N/f, (1) shows that the relative energy of waves should also depend upon the lock aspect ratio. However, for the parameter range covered by the experiments, no clear dependence upon aspect ratio was evident.

Besides the indicated errors in Figure 5, the scatter of points in the plot likely results from uncertainty in the initial conditions. The transition distance between the base of the mixed region and the underlying stratification was estimated to be as large as 2 cm in some experiments. This impacted the estimate for the APE of the lock-fluid particularly for locks with $H_m \lesssim R_c$. In addition, the

extraction of the cylinder resulted in turbulence between the lock fluid and surrounding ambient. This most significantly impacted experiments with $H_m \gtrsim R_c$. What is to be gleaned from Figures 4 and 5 is that relative energy on orders between 0.01 and 0.1 is extracted primarily by non-hydrostatic waves. Generally, the experiments provide a means to test the efficacy by which simulations performed in an axisymmetric geometry can capture the observed structure of internal waves generated by a collapsing mixed region. With well-defined initial conditions, the simulations are better able to assess the dependence of energy transport by internal waves upon rotation rate and lock aspect ratio.

III. NUMERICAL SIMULATIONS

The experimental results, particularly of relative wave energy as it depends upon Rossby number, imply that rotation significantly influences the efficiency of wave generation. However, the finite-size of the experiments constrained our analyses to times less than three buoyancy periods, which were short comparable to the rotation period. Also, by using synthetic schlieren to examine the N^2_t field, we effectively filtered low frequency waves. Thus, our experiments did not permit a thorough quantitative analysis of internal wave generation by a collapsing mixed patch.

We performed fully nonlinear numerical simulations to understand better the energetics of internal waves launched by a collapsing mixed patch. In order to perform a wide range of simulations, the equations solved by the code were restricted to an axisymmetric geometry, thus reducing the memory requirements and the number of calculations per time step. Although fine-scale non-axisymmetric structures were observed in the experiments, the macroscopic features such as the advance of the intrusion front and the structure of the generated internal waves are expected to be well captured by the code. This assertion is supported by earlier studies of non-rotating and rotating intrusions in two-layer and uniformly stratified fluid[32,40] and is further justified here through comparing the results of our simulations to the corresponding experiments. Simulations were then performed in larger domains and with wider ranging parameters including lock aspect-ratio and Rossby number.

A. Model description

The Navier-Stokes equations for axisymmetric disturbances in a Boussinesq, incompressible fluid on the f-plane is given in cylindrical coordinates by

$$
\begin{aligned}
\frac{\partial u}{\partial t} + u\frac{\partial u}{\partial r} + w\frac{\partial u}{\partial z} - \frac{v^2}{r} - fv &= -\frac{1}{\rho_0}\frac{\partial p}{\partial r} + \nu\left[\nabla^2 u - \frac{u}{r^2}\right], \\
\frac{\partial v}{\partial t} + u\frac{\partial v}{\partial r} + w\frac{\partial v}{\partial z} + \frac{uv}{r} + fu &= -\nu\left[\nabla^2 v + \frac{v}{r^2}\right], \\
\frac{\partial w}{\partial t} + u\frac{\partial w}{\partial r} + w\frac{\partial w}{\partial z} &= \frac{1}{\rho_0}\left[\frac{\partial p}{\partial z} - \rho g\right] + \nu\nabla^2 w, \\
\frac{\partial \rho}{\partial t} + u\frac{\partial \rho}{\partial r} + w\frac{\partial \rho}{\partial z} + w\frac{\partial \overline{\rho}}{\partial z} &= \kappa\nabla^2\rho, \\
\nabla \cdot \mathbf{u} &= \frac{1}{r}\frac{\partial[ru]}{\partial r} + \frac{\partial w}{\partial z} = 0,
\end{aligned}
\tag{9}
$$

where u, v, and w are the radial, azimuthal, and vertical components of velocity, g is the gravitational acceleration, ρ_0 is the characteristic density, ν is the kinematic viscosity, κ is the diffusivity, and $f = 2\Omega$ is the Coriolis parameter corresponding to a background rotation rate of Ω.

The numerical model that solves these equations is the same as that used in previous studies of non-rotating intrusive gravity currents.[32,40] Here, the effects of rotation are included. Explicitly, the code replaces the $u-$ and $w-$ momentum equations by the equation for azimuthal vorticity, $\zeta = \partial_z u - \partial_r w$,

$$
\frac{\partial \zeta}{\partial t} = -ur\frac{\partial \zeta/r}{\partial r} - w\frac{\partial \zeta}{\partial z} + \frac{1}{r}\frac{\partial[v^2 + fvr]}{\partial z} - \nu\left[\nabla^2\zeta - \frac{\zeta}{r^2}\right].
\tag{10}
$$

The discretized fields and their derivatives are computed on a staggered grid that improves stability and accuracy and also avoids the coordinate singularity at $r = 0$.

From the continuity equation for an incompressible fluid, one can define the stream function ψ, so that $\mathbf{u} = \nabla \times (\psi \hat{\theta})$. Explicitly, the components of velocity are given by $u = -\partial_z \psi$ and $w = \frac{1}{r} \partial_r (r\psi)$. Thus, the stream function is related implicitly to the azimuthal vorticity by

$$\nabla^2 \psi - \frac{\psi}{r^2} = -\zeta. \tag{11}$$

The stream function is found from the azimuthal vorticity by inverting Eq. (11) in Fourier-Bessel space and then transforming back to real-space.

Equation (10) with the v-momentum and internal energy equation in (9) are used to advance ζ, v, ρ in time. The equations were discretized using a second-order finite-difference scheme in space with free-slip boundaries. The leap-frog scheme was used to advect the equations in time with the Euler back-step every 20 time steps. For visualization purposes, a passive tracer field was also advected in time. In most simulations, particularly those run with experiment parameters, we used a time step of $\Delta t = 0.005$ s and the spatial resolution was $\Delta z = 0.48$ cm and $\Delta r = 0.31$ cm. With this resolution and time step, a typical simulation would take nearly 50 h to run as a serial process on one processor of the supercomputer cluster WestGrid, operated by ComputeCanada.

The physical parameters were taken to be constant with $g = 981$ cm/s^2, $\rho_0 = 1$ g/cm^3, and $\nu = 0.01$ cm^2/s. For salt water, the appropriate value of κ is approximately 10^{-5} cm^2/s. However, for numerical stability and efficiency, we took $\kappa = \nu = 0.01$ cm^2/s. This value is small enough that it did not influence the relevant dynamics. As with the experiments, the model was initialized with a stationary, uniformly stratified ambient fluid having buoyancy frequency N and with a region of uniform density within a radius R_c over a depth H_m from the surface. The density of this region was set to equal that of the ambient at mid-depth in the model-lock. To avoid numerical instabilities resulting from the initially abrupt change in density across the boundary between the ambient and lock-fluid, the density was set to vary smoothly radially over a small radial distance $\delta_r \simeq R_c/15$ between the lock interior and ambient. Likewise, the density varies smoothly over a small vertical distance between the base of the mixed layer and the underlying ambient.

B. Qualitative results

Figure 6 shows the snapshots from a simulation performed with the same parameters as the experiment shown in Figure 2. In particular, we show snapshots of the simulated N^2_t field at times $t = 2T_b$ and $3T_b$, which may be compared directly with the N^2_t field measured in laboratory experiments at these times, as shown in Figures 2(c) and 2(d), respectively. As in the experiments, internal waves generated beneath the collapsing region have lines of constant phase oriented at a narrow range of angles to the vertical and the amplitude of the simulated waves is comparable to
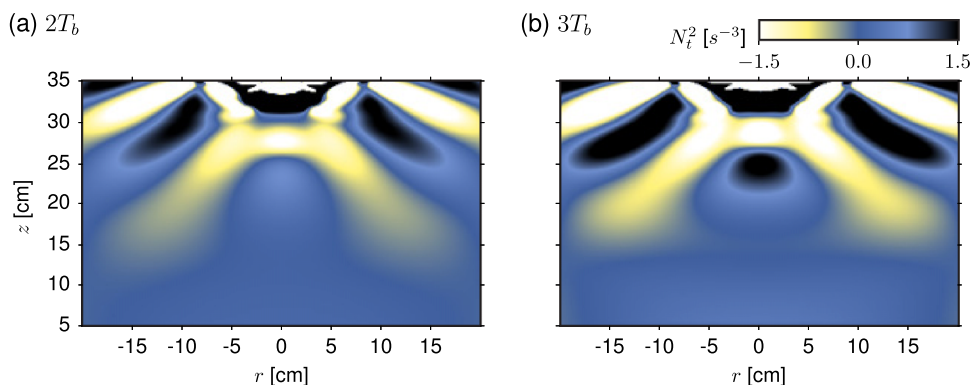

FIG. 6. Snapshots of the N^2_t field taken from numerical simulations at times (a) $t = 2T_b$ and (b) $t = 3T_b$. This simulation was initialized with the same parameters as the experiment shown in Figure 2, and the color scale used to represent values of N^2_t is the same as that in Figures 2(c) and 2(d).
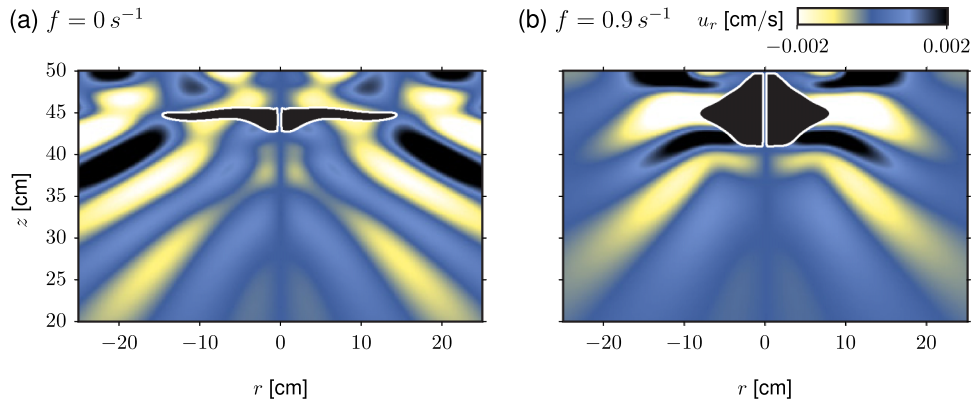
FIG. 7. The shape of the intrusion and pattern of generated internal waves at time $t = 3T_b$ in simulations with (a) no rotation and (b) $f = 0.9$ s^{-1} (Ro $\simeq 0.44$). In both cases, the ambient stratification is $N = 1.6$ s^{-1} and the initial mixed region has radius $R_c = 5$ cm and depth $H_m = 10$ cm below the surface at $z = 50$ cm. The composite image shows the radial velocity field (color field) with the passive tracer field showing the shape of the intrusion as a black region outlined by a thin white line.

that in experiments. These results provide some indication that the axisymmetric code is able to capture the dynamics observed in the laboratory experiments. Later, we will show good quantitative comparisons as well.

In order to reveal more clearly, the effect of rotation upon the evolution of the intrusion and the waves it generates, Figure 7 shows composite images of the passive tracer field, which tracks the motion of the lock-fluid, superimposed on the radial velocity field. In one simulation, there was no background rotation and in the other, the Coriolis parameter was $f = 0.9$ s^{-1}. The initial condition in both simulations was the same with a mixed region of radius $R_c = 5$ cm extending between $z = 40$ and 50 cm and having the same density as the stratified ambient at $z = 45$ cm.

The snapshots in Figure 7 are shown at $t = 3T_b$, which corresponds to approximately 1.7 inertial periods in the rotating case. At this time, qualitative differences between the non-rotating and rotating cases are clear. In the non-rotating case, the intrusion thinned as it spreads radially until it stopped due to interactions with internal waves,[32] and the waves themselves emanated at a narrow range of angles about 45° to the vertical. In the rotating case, the lock-fluid first expanded radially outward but then contracted by time $t = 3T_b$. This oscillatory expansion and contraction clearly changed the characteristics of the generated internal waves. In the case shown in Figure 7(b), the phase lines emanated nearly horizontally away from the mixed patch about the depth of the intrusion. Also apparent, however, were internal waves that propagate downward below the mixed region with phase lines oriented at angles near 45° to the vertical.

We performed a range of simulations in large domains with the lock aspect ratio fixed at $R_c/H_m = 2$ and with $N = 1.5$ s^{-1}. In most simulations, we set $f \ll N$. But we did explore one case (not shown) with $f = 1.49$ s$^{-1} \lesssim N = 1.5$ s^{-1}, in which case the mixed patch expanded and contracted as the system approached geostrophic balance, and undulations of the underlying fluid were evanescent, their amplitude decaying exponentially with vertical distance from the source.

Composite snapshots of the passive tracer and $N^2{}_t$ field taken from simulations with f ranging from 0 (no rotation) to 1.04 s^{-1} are shown in Figure 8. In all cases, internal waves were excited immediately upon the collapse of the mixed region. However, the structure of the wave field and the duration of their excitation depended upon the value of the Rossby number, given by (1).

In the absence of rotation, the lock-fluid extended radially outwards to $r \simeq 20$ cm, halting there as a consequence of interactions with internal modes.[27] In comparison to the data collected from laboratory experiments, the simulation shows that over many buoyancy periods, the collapsing mixed region excited internal waves with a wide range of frequencies made apparent by the wide-ranging slopes of phase lines from steep to shallow far from the source. But by $t = 21T_b$, the waves are no longer excited: the wavepackets have propagated away from the mixed region, but have negligible amplitude near the source itself at this time. Having spread radially away, the amplitude of the waves at this time is relatively small, with $|N^2{}_t|$ well below 0.01 s^{-3} throughout the domain.
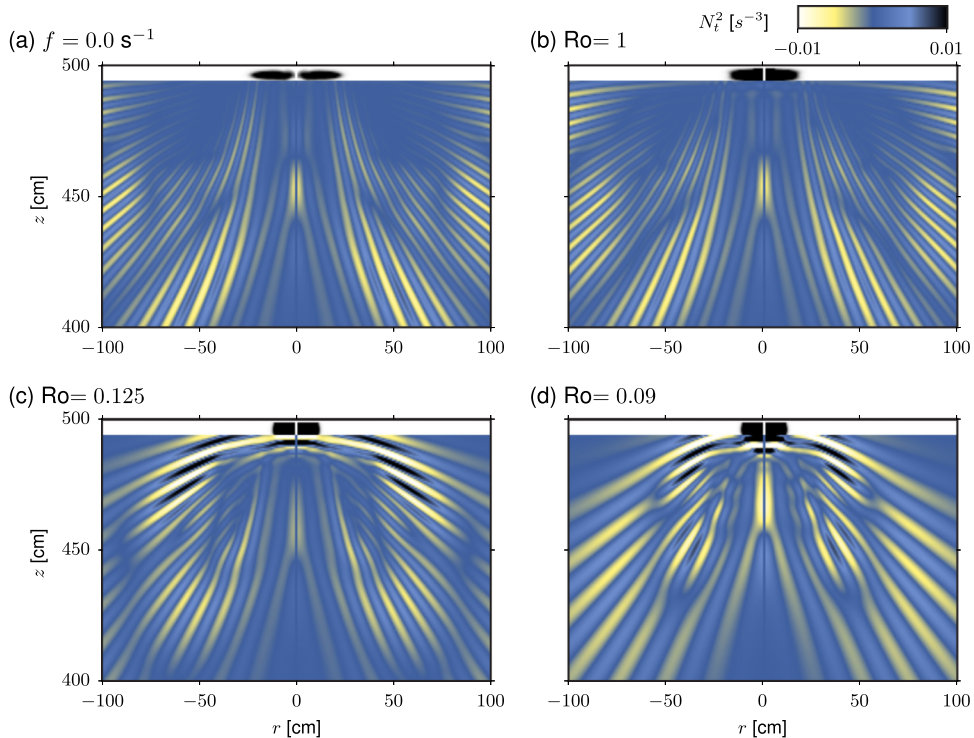
FIG. 8. Snapshots at $t = 21T_b$ (90 s) taken from simulations in a large domain with $N = 1.5$ s^{-1}, $H_m = 5$ cm, $R_c = 10$ cm and with (a) no background rotation, (b) Ro = 1 ($f \simeq 0.094$ s^{-1}), (c) Ro = 0.125 ($f \simeq 0.75$ s^{-1}), and (d) Ro = 0.09 ($f \simeq 1.04$ s^{-1}). The composite images show the N^2_t field in color below the mixed region ($z < H - H_m$) and the passive tracer field in grayscale within the mixed region ($H - H_m \leq z \leq H$). All of the figures have the same colour scale indicated in the upper right.

The effects of rotation become evident as the Rossby number reduces to Ro = 0.125 (Fig. 8(c)). In this case, the mixed region has advanced radially little beyond its initial radial extent, consistent with the deformation radius R_d being comparable to R_c. Even after $21T_b$ (about 10.5 inertial periods), internal waves continued to emanate from the base of the mixed region. In this case, the largest amplitude waves, with $|N^2_t| \simeq 0.01$ s^{-3}, had relatively shallow phase lines, corresponding to low frequency waves. In simulations with smaller Rossby number (Fig. 8(d)), low frequency waves continued to be excited below the base of the mixed region, but the vertical and radial wavelength of the disturbance far from the source was relatively larger.

For all of the Rossby numbers, the initial collapse excited downward propagating internal waves. After about two buoyancy periods, although the exact time varied depending on the Rossby number, a second wavepacket was generated. This wavepacket was distinguished from the first because the angle made by phase lines to the vertical was noticeably larger than that of the wave generated initially. In simulations with Ro $\ll 1$, internal waves were excited impulsively.

We separated the signal into two wavepackets using a Fourier band-pass filter with a frequency cutoff of $\omega = (N + f)/2$. An example of the wavepacket separation for Ro = 0.125 is shown in Figure 9. The same colour scale was used in all three images to demonstrate that the high band-pass component was of relatively large amplitude. Over time, both of the wavepackets moved down and away from the mixed region, but the direction of propagation of the low-frequency component was relatively horizontal.

As well as rotation, the structure of internal waves generated by the collapsing mixed patch depended upon the initial aspect ratio, R_c/H_m. Figure 10 shows composite images of the passive tracer field and the N^2_t field at $t = T_b$ for increasing values of the aspect ratio.

In the case with $R_c/H_m = 0.1$ (Fig. 10(a)), internal waves propagated downward from beneath the centre of the mixed region. Reducing the mixed layer depth from $H_m = 50$ to 10 cm, we found
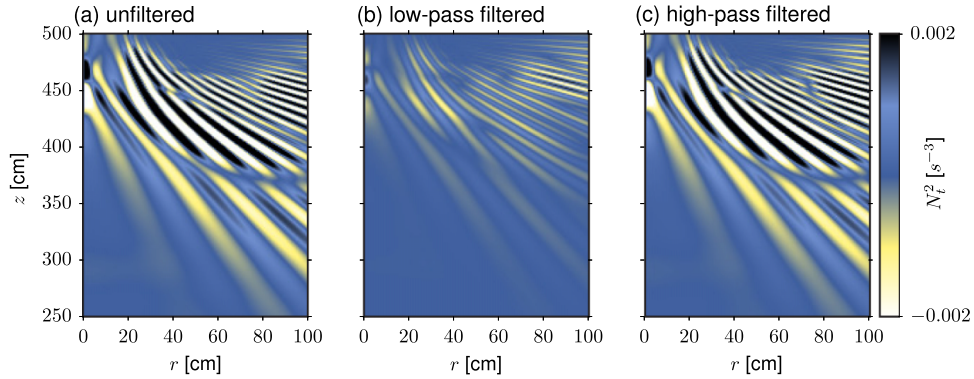
FIG. 9. (a) The N^2_t field at $t = 6T_b$ for a simulation shown in Figure 8(c), (b) the same field after passing through a low band-pass Fourier filter, and (c) the same field after passing through a high band-pass Fourier filter.

that the angle of the waves remained the same, but the horizontal and vertical wavelength and the amplitude reduced by a factor 5 (Fig. 10(b)). Further reducing H_m to 5 cm and increasing the radial extent of the mixed patch to $R_c = 100$ cm (Fig. 10(b)), it is clear that internal waves are generated below the mixed patch at its radial extremes, $r \simeq R_c$, and not directly beneath the mixed patch itself. The waves propagated downward fanning radially inward and outward about $r = R_c$. This last simulation makes it clear that the waves observed in laboratory experiments, for which $R_c \sim H_m$, involved a superposition of waves emanating from either radial extremes of the mixed patch.

C. Quantitative properties of internal waves

Following the same analysis procedure used in experiments to determine the peak frequencies, wavenumbers, and vertical displacement amplitudes associated with internal waves, we measured these characteristics for simulated internal waves.

Several simulations were run with the same parameters as laboratory experiments. Their measured frequency and radial wavenumbers are superimposed on plots of the corresponding experimental data in Figure 4(a). Although values are not identical, like the experimental data, the non-dimensional frequencies and wavenumbers lie within a narrow range $0.83 \lesssim \overline{\omega}_\star/N \lesssim 0.92$ and $2.2 \lesssim \overline{k}_\star H_m \lesssim 6.8$. The amplitudes measured from simulations are plotted together with the experimental data in Figure 4(b). Each square denotes a simulated result which is connected with the experiment to which it corresponds by a vertical grey line. Generally, we find that the amplitudes measured in simulations differed by less than 20% the amplitude measured in experiments. The discrepancy can be accounted for by experimental measurement errors, but may also be a consequence of the extraction of the cylinder in the experiments which introduces turbulence and other non-axisymmetric structures.
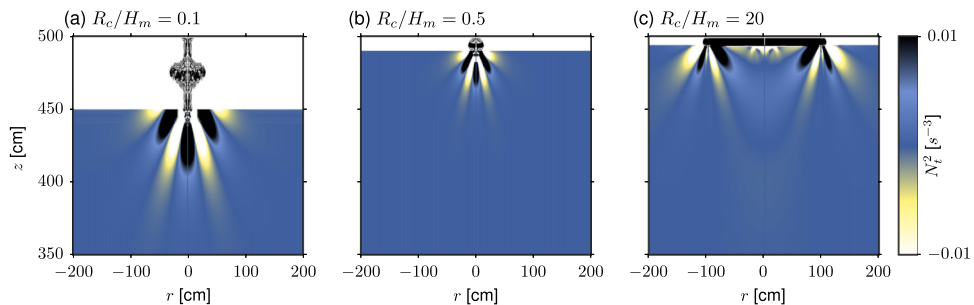

FIG. 10. As in Fig. 8 showing composite images at $t = T_b$ of the passive tracer field in the mixed region and the N^2_t field below from simulations with initial mixed-region having (a) $R_c = 5$ cm and $H_m = 50$ cm, (b) $R_c = 5$ cm and $H_m = 10$ cm, and (c) $R_c = 100$ cm and $H_m = 5$ cm. In all cases, $N = 1.5$ s^{-1} and $f = 0$ s^{-1}.
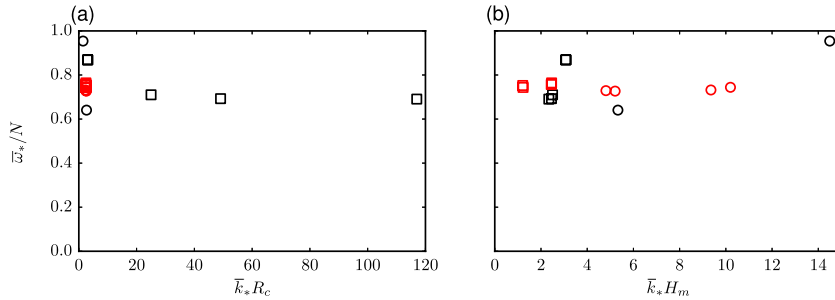
FIG. 11. From simulations with no rotation, measurements of wave frequency normalized by N versus the radial wavenumber normalized by (a) the mixed layer radius, R_c, and (b) the mixed-layer depth, H_m. The symbol shapes indicate the lock aspect ratio with circles for $R_c/H_m \leq 1$ and squares for $R_c/H_m > 1$. For black symbols, $N = 1.5$ s^{-1} was fixed and R_c/H_m varied. For red points, $R_c = 10$ cm was fixed and both H_m and N varied.

Considering the transient nature of the waves and the errors associated with the experiment measurement and analysis methods, the quantitative agreement between the numerical model and the experimental data provides promising evidence that the axisymmetric simulations well represent the dynamics of mixed region collapse from a cylindrical mixed patch.

We now go on to explore wave dynamics at parameter ranges beyond those accessible in the laboratory experiments. First, we examine the effect of the lock aspect ratio upon the frequency and radial wavenumbers in simulations with no background rotation.

Figure 11 plots the relative peak frequency against the radial wavenumber. The lock aspect ratio in the simulations ranged between $R_c/H_m = 0.1$ and 50 and the buoyancy frequency ranged between 0.75 and 3.0 s^{-1}. The wave field from three of these simulations is shown in Fig. 10.

In all cases, waves were excited in a narrow range of relative frequencies about $\bar{\omega}_\star/N \simeq 0.75$. No significant waves were observed with frequencies below 0.6 N. This result is consistent with our experiments (see Figure 4) and with previous studies of non-rotating experiments.[15]

In order to gain insight into what sets the peak radial wavenumber, Figure 11(a) plots $\bar{k}_\star$ relative to the lock radius and Figure 11(b) plots $\bar{k}_\star$ relative to the lock depth. Figure 11(a) shows that the radial wavenumber scales best with the lock radius provided the lock aspect ratio $R_c/H_m < 1$ (the data plotted as circles): $\bar{k}_\star R_c$ decreases from 3 to 1.5 as R_c/H_m decreases from 1 to 0.1. The average value of $\bar{k}_\star R_c = 2.3$ is consistent with that found in previous studies.[15] In contrast, $\bar{k}_\star R_c$ increases to 120 for high aspect-ratio locks with $1 < R_c/H_m \leq 50$ (the data plotted as squares). Fig. 11(b) shows that the radial wavenumber scales best with mixed-layer depth if the aspect ratio of the lock is high. This is anticipated because the waves are generated at the edge of the mixed region and so the radius of the mixed region plays no role in determining the properties of the waves; the waves are generated as they are from a collapsing rectilinear mixed patch.[24] Indeed, consistent with the results of rectilinear experiments, we found that $\bar{k}_* H_m$ ranged from 1.2 to 3.1 with an average value of 2.5 as R_c/H_m varied between 1 and 50. It is reasonable to expect in this case that the mixed-layer depth directly sets the vertical wavenumber of the waves and the radial wavenumber is then established through dispersion relation (6). Explicitly, if one assumes the collapsing mixed layer excites a wave with vertical wavelength $2H_m$, then setting $\omega \simeq 0.75N$, $f = 0$, and $k_z = \pi/H_m$ in (6) gives $kH_m \simeq 3.6$ of the same order as the observed relative radial wavenumbers.

Figure 12 plots the normalized vertical displacement amplitude versus lock aspect ratio determined from simulations with no rotation. For low aspect-ratio locks, the amplitude was small, with $|\bar{\xi}|_* \simeq 0.03H_m$ for $R_c/H_m = 0.1$. For high aspect-ratio locks, the relative amplitude was much larger. In a range of simulations with $H_m = 5$ cm fixed and with varying $R_c > H_m$, we found $|\bar{\xi}|_* \simeq 0.12H_m$, increasing moderately as R_c/H_m increased from 10 to 50. Laboratory experiments of rectilinear intrusions suggested that the wave amplitude should increase approximately as the cube of the mixed-layer depth. With our focus here upon effects of aspect ratio and rotation, we did not examine in detail the dependence of wave amplitude upon mixed-layer depth in non-rotating simulations.
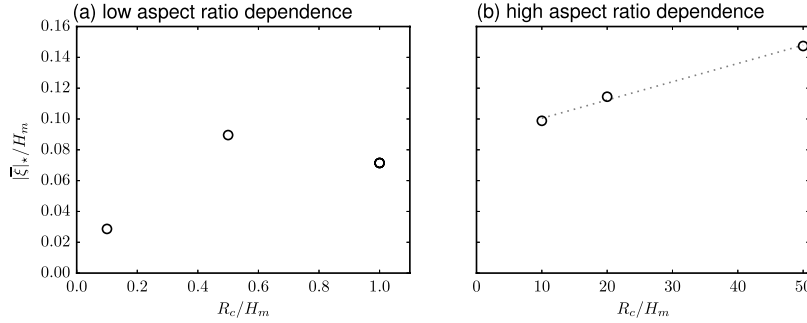
FIG. 12. Relative maximum vertical displacement amplitudes plotted against the lock aspect ratio shown separately for simulations with (a) low aspect-ratio locks with $R_c/H_m \leq 1$ and (b) high aspect-ratio locks with $R_c/H_m \geq 10$. The best-fit line is shown for $R_c/H_m \geq 10$ as a gray dotted line in (b).

We now turn to the examination of waves in simulations with the effects of background rotation included. Time series of the simulated wave field over the first three buoyancy periods were Fourier high-pass and low-pass filtered and from these fields, the peak frequencies were determined. These frequencies relative to N and f were represented by the angle θ using (5), as plotted in Figure 13(a). The plot of $\sin\theta$ versus $\cos\theta$ shows a separation between the characteristic frequency associated with each of the wavepackets into near-inertial waves (for which $\theta \lesssim \pi/2$, $\omega \gtrsim f$) and non-hydrostatic waves (for which $\theta \gtrsim 0$, $\omega \lesssim N$).

Figure 13(b) considers how the radial wavenumber changes for high- and low-frequency waves between early times ($T_b < t < 3T_b$) and moderate times ($3T_b < t < 6T_b$). At early times in all simulations, the characteristic wavenumbers of the near-N and near-f waves were exactly $\overline{k}_\star = 0.64$ cm^{-1} and $\overline{k}_\star = 0.49$ cm^{-1}, respectively. At times between $3T_b$ and $6T_b$, the measured wavenumbers spanned a wider range but were generally smaller for high- and low-frequency wavepackets.

There was a noticeable partition in the amplitude of high- and low-frequency waves. Figure 14 shows that the near-N waves had vertical displacement amplitudes around 1.4% of the initial mixed-layer depth in simulations with Rossby numbers as low as Ro = 0.4. The amplitude was significantly smaller for Ro $\lesssim 0.1$. In contrast, the near-inertial waves had much smaller amplitudes, around 0.3% of the mixed-layer depth, though there was no significant change in the amplitude as it depended upon Rossby numbers between 0.09 and 1. The smaller vertical displacement amplitudes are to be expected because low-frequency waves move predominantly in the horizontal.

D. Energy transport

Because the simulations can be run in large domains, we are better able to assess the transport of energy by downward propagating internal waves over short and long times. As with the laboratory
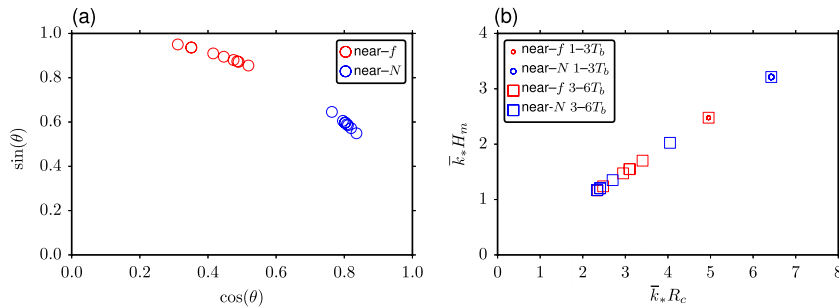

FIG. 13. (a) Simulated relative peak frequencies for $t < 3T_b$ associated with the high- and low-frequency band-pass filtered wavepackets as represented by θ, defined by (5). (b) The corresponding radial wavenumbers at early and late times for high- and low-frequency band-pass filtered wavepackets. In all cases, $N = 1.5$ s^{-1}, $H_m = 5$ cm, $R_c = 10$ cm and Ro ranges from 0.09 to 1.
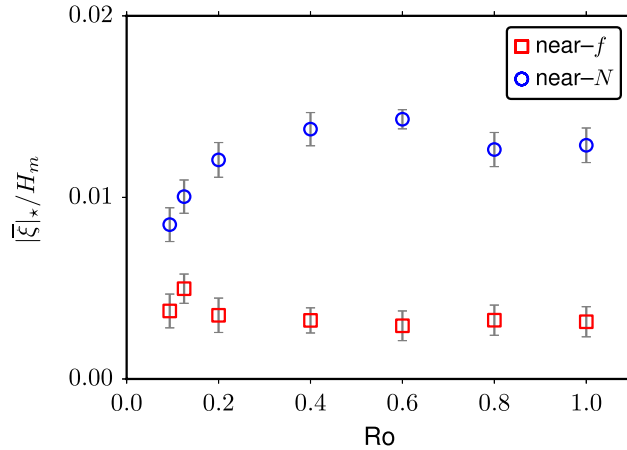
FIG. 14. Normalized vertical displacement amplitudes measured from simulations at times about $t = T_b$ plotted against Rossby number. Simulation parameters are the same as those in Figure 13.

experiments, the energy was computed from the energy flux across a horizontal area just below the mixed region and integrating this over different time intervals. The histograms in Figure 15 show the fraction of the initial available potential energy transported by near-inertial waves and by non-hydrostatic waves as it depended upon the Rossby number. In Fig. 15(a), the extracted energy is evaluated over the first 3 and 6 characteristic periods of the inertial waves and it is evaluated over long times up to $21T_b$. Likewise, Fig. 15(b) shows the extracted energy from over the first 3 and 6 characteristic periods of the non-hydrostatic waves and over $21T_b$.

For Ro $\gtrsim 1$, near-inertial waves extracted nearly 100% of the total extracted energy over the first 6 wave periods. For smaller Ro, waves were excited over longer times so that, for example, only 65% of the total energy associated with inertial waves was transported by these waves over time $t = 6T_w$. The largest fraction of energy transported by inertial waves occurred in the simulation with Ro = 0.125. This result is consistent with other numerical studies of collapsing mixed regions in stratified fluids.[33,41] With our definition (1) of the Rossby number, the case Ro = 0.125 corresponds to the deformation radius being equal to the initial radius of the mixed patch: $R_d \simeq R_c$. In this case, the mixed region collapsed most efficiently, converting available potential to kinetic energy and generating a single geostrophically balanced lens.[33]

In all cases, we found that non-hydrostatic internal waves extracted an order of magnitude larger fraction of energy than the near-inertial waves, with values of the same order as those observed in the laboratory experiments (see Figure 5). Almost all the energy was extracted during the first 6 wave periods except in the case with Ro = 0.09. This case was also exceptional in that the total fraction of extracted energy was as large as 5% of the initial available potential energy.
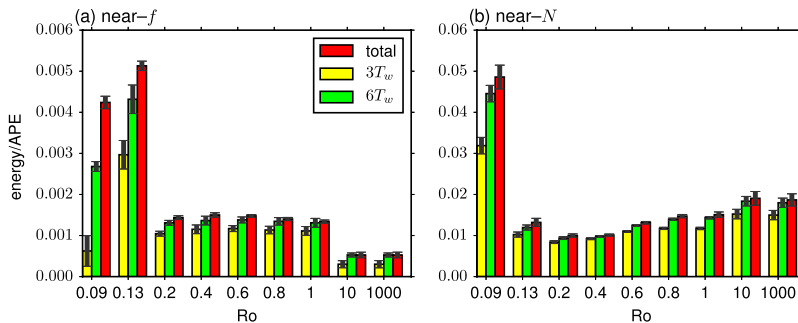

FIG. 15. Bar graphs showing the relative energy released after $t = 3T_w$, $6T_w$, and $21T_b$ (90 s) for (a) the near-inertial waves and (b) non-hydrostatic waves. The simulations were run with the fixed parameters given in Figure 13 and with a range of f. Errors indicated in gray at the top of each bar represent the standard deviation of measurements of energy across a range of horizontal levels between 4 and 6 cm below the base of the mixed region.

That significant energy was transported by waves with frequencies near N even in simulations with low Rossby numbers indicates that the near-inertial undulations of the geostrophically adjusting mixed patch also acted impulsively to launch non-hydrostatic waves during each cycle. This assertion is further supported by the observation that a non-negligible fraction of energy continued to be transported away by non-hydrostatic waves even after $t = 6T_w$.

Because the aspect ratio of the mixed patch was near unity in these simulations, the results cast the relative energy transport in terms of the initial available potential energy of the whole mixed patch. For high aspect-ratio locks ($R_c/H_m \gg 1$), it would be better to relate the transported energy to the available potential energy over an annulus with radius equal to the circumference of the mixed patch and width equal to one deformation radius.

IV. DISCUSSION AND CONCLUSIONS

An earlier experimental investigation into the generation of downward propagating internal waves resulting from the collapse of a cylindrical mixed region in uniformly stratified fluid[15] has been extended both through experiments and numerical simulations to examine the influence of rotation and the initial aspect ratio of the mixed region upon the structure and energetics of the waves.

For waves generated by the release of mixed fluid from low aspect-ratio locks, their spatial structure and amplitude were set by the height of the mixed region such that $\overline{k}_\star = 2.5H_m^{-1}$ and $|\overline{\xi}|_\star \simeq 0.1H_m$. For very wide mixed regions, wave excitation occurred only at the radial extreme of the mixed region indicating that the circumference rather than the horizontal area of the mixed patch dictates the energy transported by the waves. Although the experiments with rotation showed that the waves were generated with a narrow range of frequencies moderately below N, the simulations showed an additional peak frequency occurred near f, though the energy associated with these near-inertial waves was much smaller than that of the non-hydrostatic waves. Inertial waves transported the most energy in simulations for which the radius of the mixed region was comparable to the deformation radius. The energy transported by non-hydrostatic waves increased for Rossby numbers as low as 0.09 and these waves were continually, though impulsively, excited over many wave periods by the geostrophically adjusting mixed patch.

We did not examine circumstances more representative of oceanic scales because of the high computational cost required by our direct numerical simulation. However, the results presented here can be used to make a crude prediction of the energetics of internal waves excited by the collapse mixed region formed by a storm above.

As in Ref. 15, we consider the cold water wake left by Hurricane Edouard.[18] This had depth $H_m \simeq 50$ m and an across-track aspect ratio of $R_c/H_m \simeq 4000$. Taking the surrounding ambient to have a characteristic stratification[42,43] of $N = 0.005$ s^{-1} and supposing $f/N \simeq 0.01$, the deformation radius was $R_d \simeq 5$ km and the Rossby number given in terms of the half-width of the wake was Ro $\simeq 3 \times 10^{-3}$.

Our results suggest that shortly after formation of the wake, energy would be transported away from its flanks predominantly by non-hydrostatic internal waves with frequencies around 0.004 s^{-1} and with radial and vertical wavelengths around $2H_m \simeq 100$ m. The vertical displacement amplitude is expected to be less than a half a meter. All of this is to say that the waves are expected to be generated at such small spatial and temporal scales as to avoid obvious detection by present ocean instruments.

Based upon ocean observations,[20] we suppose that a hurricane increases the available potential energy of the mixed layer at a rate of 0.1 TW. Only a fraction of this residing on the margins of the mixed patch can go into internal wave generation. Multiplying by the ratio of R_d to the half-width of the wake gives an initial available potential energy input per time of $\simeq 3$ GW. Based upon the results of our simulations with Ro = 0.09, we suppose that 5% of this power, $\simeq 0.2$ GW, is extracted from mixing due to a passing hurricane by non-hydrostatic internal waves. Considering that there are about 50 hurricanes per year,[18] we estimate the annual average power input from tropical cyclones to internal waves though the collapse of the mixed region in its wake is approximately 10 GW. This

is of the same order of magnitude as the estimate of Nilsson[9] for the power transported horizontally away by near inertial waves propagating along the thermocline. But it is an order of magnitude smaller than estimates of the power associated with oceanic internal waves generated directly by surface wind stress.[44]

Having focused our scaling analysis using data from hurricanes, we have neglected possible contributions from internal waves generated by collapsing mixed patches from smaller but more frequently occurring storms over the oceans. Having neglected local circulations within the mixed region induced by surface wind stresses, our simplified model is not intended to be truly predictive. Rather, it has shown that the energetics associated with internal waves excited by a collapsing mixed patch are not insignificant.

Our results are more directly applicable to pervasive patches of localized turbulent mixing in the ocean interior that have aspect ratios between[7] 10 and 1000. We have shown that these patches generate downward propagating waves that can transport energy to greater depth. The succession of wave breaking, creating a mixed patch and a mixed patch collapsing to excite waves constitutes a previously unexplored mechanism for energy to cascade from large to small scale.

Future work will consider the effect of wind stress-induced circulations non-axisymmetric phenomena, such as the occurrence of baroclinic instability,[28,45] upon the excitation of internal waves below a collapsing mixed patch in rotating stratified fluid.

ACKNOWLEDGMENTS

[1] W. H. Munk, "Abyssal recipes," Deep-Sea Res. Oceanogr. Abstr. **13**, 707–730 (1966).

[2] W. H. Munk and C. Wunsch, "Abyssal recipes II: Energetics of tidal and wind mixing," Deep Sea Res., Part I **45**, 1977–2010 (1998).

[3] C. Wunsch and R. Ferrari, "Vertical mixing, energy, and the general circulation of the oceans," Annu. Rev. Fluid Mech. **36**, 281–314 (2004).

[4] R. Ferrari and C. Wunsch, "Ocean circulation kinetic energy: Reservoirs, sources, and sinks," Annu. Rev. Fluid Mech. **41**, 253–282 (2009).

[5] K. L. Polzin, J. M. Toole, J. R. Ledwell, and R. W. Schmitt, "Spatial variability of turbulent mixing in the abyssal ocean," Science **276**, 93–96 (1997).

[6] N. S. Oakey and B. J. W. Greenan, "Mixing in a coastal environment: 2. A view from microstructure measurements," J. Geophys. Res. **109**, C10014, doi:10.1029/2003JC002193 (2004).

[7] M. A. Sundermeyer, J. R. Ledwell, N. S. Oakey, and B. J. W. Greenan, "Stirring by small-scale vortices caused by patchy mixing," J. Phys. Oceanogr. **35**, 1245–1262 (2005).

[8] G. D. Egbert and R. D. Ray, "Significant dissipation of tidal energy in the deep ocean inferred from satellite altimeter data," Nature **405**, 775–778 (2000).

[9] J. Nilsson, "Energy flux from traveling hurricanes to the oceanic internal wave field," J. Phys. Oceanogr. **25**, 558–573 (1995).

[10] K. Dohan and R. E. Davis, "Mixing in the transition layer during two storm events," J. Phys. Oceanogr. **41**, 42–66 (2011).

[11] K. Dohan and B. R. Sutherland, "Internal waves generated from a turbulent mixed region," Phys. Fluids **15**, 488–498 (2003).

[12] K. Dohan and B. R. Sutherland, "Numerical and laboratory generation of internal waves from turbulence," Dyn. Atmos. Oceans **40**, 43–56 (2005).

[13] J. R. Munroe and B. R. Sutherland, "Internal wave energy radiated from a turbulent mixed layer," Phys. Fluids **26**, 096604 (2014).

[14] V. S. Maderich, G. J. F. van Heijst, and A. Brandt, "Laboratory experiments on intrusive flows and internal waves in a pycnocline," J. Fluid Mech. **432**, 285–311 (2001).

[15] A. M. Holdsworth, S. Decamp, and B. R. Sutherland, "The axisymmetric collapse of a mixed patch and internal wave generation in uniformly stratified fluid," Phys. Fluids **22**, 106602 (2010).

[16] W. R. Boos, J. R. Scott, and K. A. Emanuel, "Transient diapycnal mixing and the meridional overturning circulation," J. Phys. Oceanogr. **34**, 334–341 (2003).

[17] R. L. Sriver and M. Huber, "Observational evidence for an ocean heat pump induced by tropical cyclones," Nature **447**, 577–580 (2007).

[18] K. Emanuel, "Contribution of tropical cyclones to meridional heat transport by the oceans," J. Geophys. Res. **106**, 14771–14781, doi:10.1029/2000JD900641 (2001).

[19] E. D'Asaro, P. Black, L. Centurioni, P. Harr, S. Jayne, I.-I. Lin, C. Lee, J. Morzel, R. Mrvaljevic, P. P. Niiler, L. Rainville, T. Sanford, and T. Y. Tang, "Typhoon-ocean interaction in the Western North Pacific: Part 1," Oceanography **24**, 24–31 (2011).

[20] L. L. Liu, W. Wang, and R. X. Huang, "The mechanical energy input to the ocean induced by tropical cyclones," J. Phys. Oceanogr. **38**, 1253 (2008).

[21] M. C. Gregg, "Finestructure and microstructure observations during the passage of a mild storm," J. Phys. Oceanogr. **6**, 528–555 (1976).

[22] J. F. Price, "Upper ocean response to a hurricane," J. Phys. Oceanogr. **1**, 153–175 (1981).

[23] B. R. Sutherland, M. R. Flynn, and K. Dohan, "Internal wave excitation from a collapsing mixed region," Deep Sea Res., Part II **51**, 2889–2904 (2004).

[24] B. R. Sutherland, A. N. F. Chow, and T. P. Pittman, "The collapse of a mixed patch in stratified fluid," Phys. Fluids **19**, 116602 (2007).

[25] J. R. Munroe, C. Voegeli, B. R. Sutherland, V. Birman, and E. H. Meiburg, "Intrusive gravity currents from finite-length locks in a uniformly stratified fluid," J. Fluid Mech. **635**, 245–273 (2009).

[26] B. D. Maurer, D. T. Bolster, and P. F. Linden, "Intrusive gravity currents between two stably stratified fluids," J. Fluid Mech. **647**, 53–69 (2010).

[27] A. M. Holdsworth and B. R. Sutherland, "Influence of lock aspect ratio upon the evolution of an axisymmetric intrusion," J. Fluid Mech. **735**, R3 (2013).

[28] R. W. Griffiths, "Gravity currents in rotating systems," Annu. Rev. Fluid Mech. **18**, 59–89 (1986).

[29] M. Ungarish and H. E. Huppert, "The effects of rotation on axisymmetric gravity currents," J. Fluid Mech. **362**, 17–51 (1998).

[30] M. A. Hallworth, H. E. Huppert, and M. Ungarish, "Axisymmetric gravity currents in a rotating system: Experimental and numerical investigations," J. Fluid Mech. **447**, 1–29 (2001).

[31] M. Ungarish and T. Zemach, "On axisymmetric rotating gravity currents: Two-layer shallow-water and numerical solutions," J. Fluid Mech. **481**, 37–66 (2003).

[32] A. M. Holdsworth, K. J. Barrett, and B. R. Sutherland, "Axisymmetric intrusions in two-layer and uniformly stratified environments with and without rotation," Phys. Fluids **24**, 036603 (2012).

[33] M.-P. Lelong and M. A. Sundermeyer, "Geostrophic adjustment of an isolated diapycnal mixing event and its implications for small-scale lateral dispersion," J. Phys. Oceanogr. **35**, 2352–2367 (2005).

[34] G. Oster, "Density gradients," Sci. Am. **213**, 70 (1965).

[35] J.-B. Flor, M. Ungarish, and J. Bush, "Spin-up from rest in a stratified fluid: Boundary flows," J. Fluid Mech. **472**, 51–82 (2002).

[36] D. Bolster, A. Hang, and P. F. Linden, "The front speed of intrusions into a continuously stratified medium," J. Fluid Mech. **594**, 369–377 (2008).

[37] S. B. Dalziel, G. O. Hughes, and B. R. Sutherland, "Whole field density measurements," Exp. Fluids **28**, 322–335 (2000).

[38] B. R. Sutherland, M. R. Flynn, and K. Onu, "Schlieren visualisation and measurement of axisymmetric disturbances," Nonlinear Processes Geophys. **10**, 303–309 (2003).

[39] M. R. Flynn, K. Onu, and B. R. Sutherland, "Internal wave generation by a vertically oscillating sphere," J. Fluid Mech. **494**, 65–93 (2003).

[40] J. M. McMillan and B. R. Sutherland, "The lifecycle of axisymmetric internal solitary waves," Nonlinear Processes Geophys. **17**, 443–453 (2010).

[41] G. A. Stuart, M. A. Sundermeyer, and D. Hebert, "On the geostrophic adjustment of an isolated lens: Dependence on Burger number and initial geometry," J. Phys. Oceanogr. **41**, 725–741 (2011).

[42] R. Pinkel and S. Anderson, "Shear, strain, and Richardson number variations in the thermocline. Part I: Statistical description," J. Phys. Oceanogr. **27**, 264–281 (1997).

[43] C. Ladd and L. A. Thompson, "Formation mechanisms for North Pacific central and eastern subtropical mode waters," J. Phys. Oceanogr. **30**, 868–887 (2000).

[44] R. Ferrari and C. Wunsch, "The distribution of eddy kinetic and potential energies in the global ocean," Tellus A **62**, 92–108 (2010).

[45] R. W. Griffiths and P. F. Linden, "Laboratory experiments on fronts," Geophys. Astrophys. Fluid Dyn. **19**, 159–187 (1982).